COBEM 2023 27TH INTERNATIONAL CONGRESS OF MECHANICAL ENGENEERING

ABCM Brazilian Society of Mechanical Sciences and Engineering
27th ABCM International Congress of Mechanical Engineering
December 04-08, 2023, Florianópolis-SC, Brazil

COB-2023-2405
HIGH-ENTROPY ALLOY CrMnFeNiCu: A CHARACTERIZATION AND APPLICATION STUDY

Catarina Meiko Hayashi
Daniel Fonseca Cunha
PPGMAT – EMC – CTC – Universidade Federal de Santa Catarina, Florianópolis, Santa Catarina, CEP 88040-900, Brazil.
hayashi.h@posgrad.ufsc.br
daniel.cunha@ufsc.br

Manoel Kolling Dutra
LMP – Precision Engineering Laboratory – EMC – CTC – Universidade Federal de Santa Catarina. Florianópolis, Santa Catarina, CEP 88040-900, Brazil.
manoel.kolling@posgrad.ufsc.br

Francielen Pujol Nobre
Engenharia de Materiais – EMT – Universidade Federal de Santa Catarina, Blumenau, Santa Catarina, CEP 89036-256, Brazil.
francielen.pujol@grad.ufsc.br

Athos Fernandes Araújo
Felipe Martina André
Claudio Michel Poffo
PPGMAT – EMC – CTC – Universidade Federal de Santa Catarina, Florianópolis, Santa Catarina, CEP 88040-900, Brazil.
athos.araujo@posgrad.ufsc.br
felipe.martina@posgrad.ufsc.br
claudio.poffo@ufsc.br

Throughout history alloying has proven that synergistic effects can provide innovative properties to metallic materials. With this motivation, high entropy alloys (HEAs) have been studied in recent years. These alloys are designed with at least five elements in varying proportions (most recently non-equimolar) to attain thermodynamic stability of simple phases with aleatory atomic distribution. The HEA system CrMnFeNiCu (chrome, manganese, iron, nickel, and copper) has been synthesized by mechanical alloying and deposited by laser cladding. The characterization by x-ray diffraction indicates, in early milling hours, the coexistence of BCC (body centered cubic) and FCC (face centered cubic) phases. Further characterization shows the evolution of these phases and an increased crystalline fraction in the as-milled nanostructured HEA. Differential scanning calorimetry indicates heat capacity of 0.5984 J/gK at room temperature. Morphology observed in optical microscopy reveals a fine structure with biphasic composition and a homogenous dispersion of precipitated particles at 2500 W, reaching an average Vickers hardness of 389.5 HV.

Keywords: *high entropy alloy, mechanical alloying, laser cladding, XRD, DSC.*

1. INTRODUCTION

High entropy alloys (HEAs) are multicomponent alloys with more than two principal elements (ideally five or more), with 1st generation HEAs being mostly single phase equimolar and 2nd generation having diverse mixture fractions and multiphase microstructure (Arif *et al.*, 2022). The properties observed in HEAs are strongly related to four core effects: high entropy, severe lattice distortion, sluggish diffusion, and "cocktail". High entropy of mixture improves stability of the HEA phases and promotes the formation of simpler structures (cubic, hexagonal) instead of complex ones (trigonal, triclinic) with intermetallic precipitations. The random distribution of atoms inside the structure promotes severe lattice distortion by differences in atomic radii, altering phonon and electron motion, and changing diffusion potential energy. The cocktail effect represents the synergistic properties observed in HEAs, which can go beyond the properties of individual alloy components (Murty *et al.*, 2019).

Mechanical alloying is a common powder production route for HEAs. This solid-state processing technique promotes cold welding and fracturing through shear and collisions. A homogeneous mixture is obtained in early milling times followed by particle welding, fracturing, and phase growth as time increases. After phase growth reaches equilibrium, nanostructures start to form by accumulation of defects in grain boundaries and grains decrease in size. The resulting nanostructure comprises of nanosized grains surrounded by interfacial regions (Kumar *et al.*, 2022). The HEA

powder can then be consolidated through different methods, being laser cladding (LC) one of the usually reported practices (Arif *et al.*, 2022; Murty *et al.*, 2019).

Laser deposition by LC allows the application of HEAs as coatings, aiming to create a function gradient by improving surface hardness and chemical resistance while preserving substrate integrity and properties. Power and scan speed are critical parameters to control LC-HEA microstructure and defects, therefore proper parameter selection can provide melt zones with low dilution and pore count, preserving of both HEA and substrate properties (Arif *et al.*, 2022; Murty *et al.*, 2019).

2. METHODOLOGY

The CrMnFeNiCu equimolar HEA has been synthesized by MA in a high energy mill using ball per powder ratio (BPR) 7:1 and commercial grade elemental powders (>99.3% purity). A stainless-steel milling jar containing 41.1510 g of 304 stainless-steel milling balls and 5.8788 g of elementary powder mix was sealed with argon (Ar) to reduce oxidation effects. The milling process was executed for 5 h, with cooling intervals of 5 min every 30 min to control temperature and mitigate intermetallic segregation. No lubricants or additives were applied. During the milling process 10 mg samples were removed for differential scanning calorimetry (DSC) and the powder was subjected to x-ray diffraction (XRD). After 5 h of milling, the synthesized HEA powder was pre-deposited on a 1020 steel plate and laser cladded by a Nd:YAG laser using three power settings (1500 W, 2000 W and 2500 W), scanning speed of 5 mm/s and spot diameter of 1.2 mm.

2.1 Analytical procedures for thermal and structural properties

To evaluate thermal behavior and properties, differential scanning calorimetry (DSC) was executed at every milling hour. The temperature scanning range was 313,15 K to 803,15 K with heating rate of 10 K/min under nitrogen (N_2) atmosphere. In addition, a DSC test was made at temperature range 273,15 K to 373,15 K to determine the HEA specific heat (C_p) at 25 °C, based on ASTM E1269 (ASTM, 2018), using sapphire heat flow standard and aluminum (Al) sample holder (pan), as shown in Eq. (1):

$$C_{p,sample} = \frac{m_{std}}{m_{sample}} \times \frac{\varphi_{sample} - \varphi_{pan}}{\varphi_{std} - \varphi_{pan}} \times C_{p,std} \quad (1)$$

where $C_{p,sample}$ and $C_{p,std}$ are the calculated HEA C_p (J/gK) and sapphire standard C_p, respectively; m_{std} and m_{sample} are the sapphire standard and HEA sample masses (mg), respectively; φ_{sample}, φ_{std} and φ_{pan} are the HEA sample, sapphire standard and Al pan detected heat flow (mW), respectively.

X-ray diffraction (XRD) using Cu-K_α radiation (λ = 1,5406 Å) took place during 2 h and 5 h milling times to analyze phase formation and evolution. The experimental diffraction data was then compared to information available at the Inorganic Crystal Structure Database (ICSD) (Zagorac *et al.*, 2019). The crystal structure was refined by the Rietveld method using the General Structure Analysis System (GSAS) software (Larson and Von Dreele, 2000) to quantify phase fractions and, with the refined data, the average crystallite size was measured using peak geometry and Scherrer's formula, as per Eq. (2):

$$C_s = \frac{0.9\lambda}{FWHM \times \cos(\theta_{FWHM})} \quad (2)$$

where C_s is the average crystallite size, λ is the x-ray wavelength (nm), $FWHM$ is the full width at half maximum of a diffraction peak (rad) and θ_{FWHM} is peak center angle (2θ, degree) (Cullity and Stock, 2014).

2.2 Morphology evaluation and mechanical properties

The applied LC-HEA had its microstructural features investigated by optical microscopy (OM). Samples were cut from the cross-section for each power input and longitudinal section of the transition zones, as shown in Figure 1. Vickers microhardness tests were made in each cross-section to investigate properties of the melted zone (MZ), heat affected zone (HAZ), and substrate (in regions A, B and C), following the ASTM E384 standard specifications (ASTM, 2022).

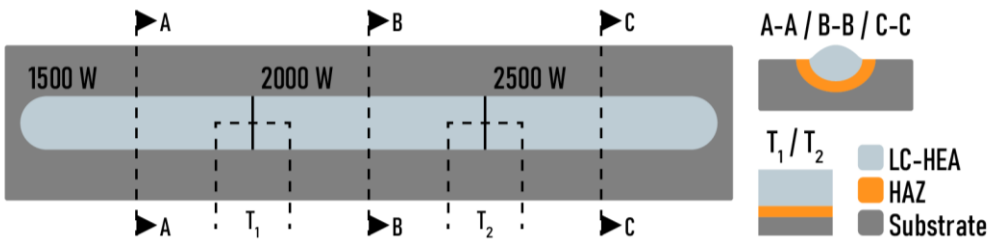

Figure 1. Schematic indication of sampling regions of the LC-HEA and zones of interest in the cross-section geometry.

3. RESULTS AND DISCUSSIONS

With the synthesis of the CrMnFeNiCu HEA two sets of results were obtained. The first one comprising an investigation of phase formation by mechanical synthesis route of high energy milling (MA) and as-milled MA-HEA thermal properties; the second one being the application of the 5 h MA-HEA as feedstock material for laser cladding (LC) and evaluation of the resulting LC-HEA microstructure post-melting, its interface with the substrate, and as-cladded mechanical properties.

3.1 Mechanical alloying results

The DSC curves shown in Figure 2(a) indicate that the samples have a generally similar exothermal behavior (broad peak centered around 746 K) with nuances around 408 K range and, in early milling hours, endothermic peaks can be identified around 540 K. MA creates heavy structural stress due to cold welding and deformation, this energy is then released during the analysis forming the broad exothermic band indicated around 746 K (Shkodich *et al.*, 2022).

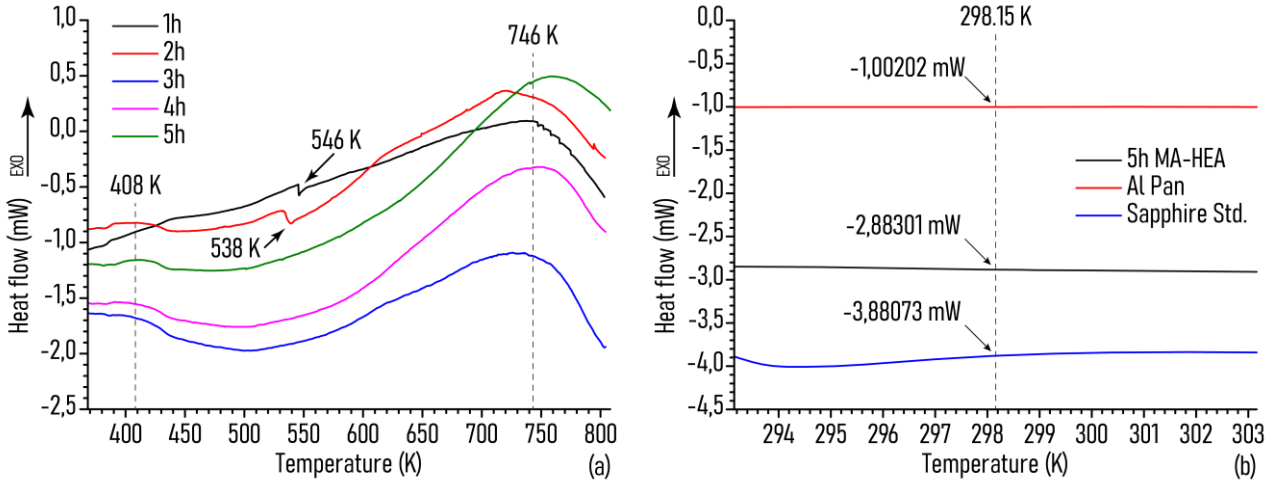

Figure 2. DSC curves from MA-HEA sampled hourly (a) and Cp determination at 298,15 K based on ASTM E1269 (b).

The two endothermic bands near 538 K and 546 K, are believed to be martensitic transformations (Saud *et al.*, 2014). As milling continues, these transformations stop occurring, most likely due to structural changes, as the HEA is formed, and the nanostructure becomes more prevalent. From 2 h onwards a broad band appears around 408 K indicating crystallite growth (Ni *et al.*, 2019). After this point (3 h) the MA-HEA appears to stabilize, and curves become more like each other.

To determine the MA-HEA C_p according to ASTM E1269, the heat flow data from a 5 h sample was compared to a standardized sapphire calibration sample as well as the Al pan (empty sample holder), the results are shown in Figure 2(b). The methodology proposed by the ASTM is based on DSC analysis theory, therefore being a reliable and expedient experimental approach for quick evaluations (Höhne *et al.*, 2003; ASTM, 2018).

Applying the analytical data to Eq. (1) we obtain the results presented in Eq. (3)

$$C_{p,sample} = \frac{12.30\ mg}{10.40\ mg} \times \frac{(-2.88301)-(-1,00202)\ mW}{(-3.88073)-(-1,00202)\ mW} \times 0.7744\ J/gK\ = 0.5984\ J/gK \quad (1)$$

This value can be compared with a weighted average specific heat of the mixture ($C_{p,Mix}$) for this HEA composition, CrMnFeNiCu, as indicated in Eq. (4):

$$C_{p,Mix} = \frac{0.20\times C_{p,Cr}+0.20\times C_{p,Mn}+0.20\times C_{p,Fe}+0.20\times C_{p,Ni}+0.20\times C_{p,Cu}}{1.00} \quad (4)$$

where $C_{p,Cr} = 0.449$ J/gK, $C_{p,Mn} = 0.479$ J/gK, $C_{p,Fe} = 0.445$ J/gK, $C_{p,Ni} = 0.439$ J/gK and $C_{p,Cu} = 0.385$ J/gK are the specific heat of the alloying elements from the sample HEA. With $C_{p,Mix} = 0.439$ J/gK and $C_{p,sample} = 0.5984$ J/gK we can verify an increase in the HEA properties that is superior to the average of the isolated elements, as expected by the cocktail effect (Murty *et al.*, 2019).

XRD analysis were executed at 2 h and 5 h, the normalized data is presented in Figure 3(a) and non-normalized in Figure 3(b) for comparison. At first glance, the superposition of the diffraction peaks indicate that two phases are present, and the structure remains stable during the process.

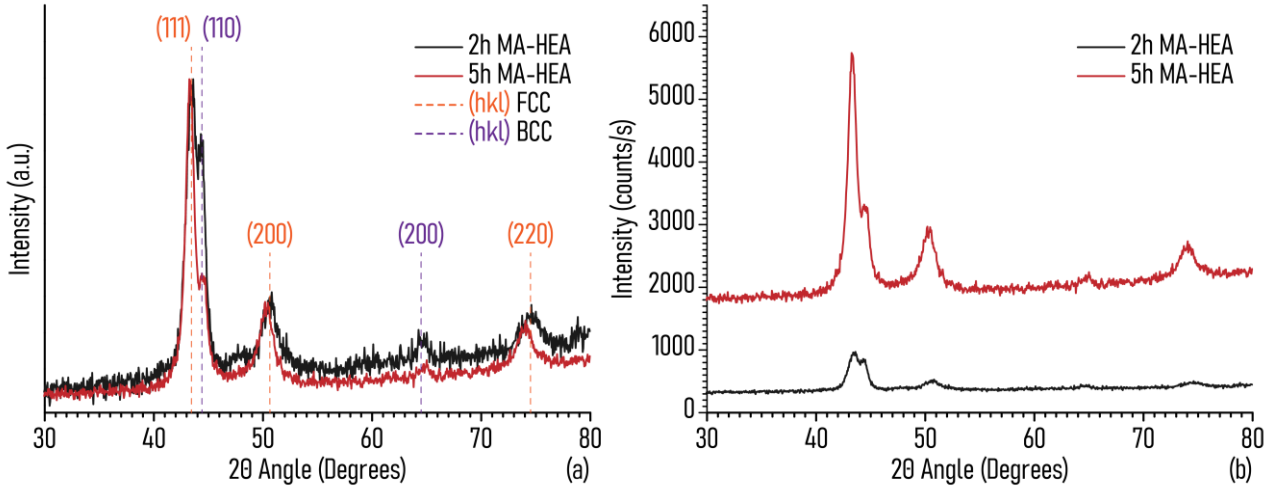

Figure 3. Normalized (a) and regular (b) diffractograms from the MA-HEA, with 2 h and 5 h milling times. Peaks indicated in 2θ degrees correspond to BCC (44.40 ° and 64.62 °) and FCC (43.43 °, 50.63 ° and 74.61 °) phases.

The BCC phase with peaks at 44.40 ° and 64.62 ° were identified using the ICSD index no. 108378, an equimolar CuFeNi alloy with spatial group F m -3 m (Bradley *et al*, 1941), and the FCC phase with peaks at 43.43 °, 50.63 °, and 74.61 ° were identified using the ICSD index no. 44731, a Cr phase study with spatial group I m -3 m (Straumanis and Weng, 1956). Modifications were made to the ICSDs cards to address the difference in composition, adding the remaining solution elements.

Crystal structure refinement was executed using these modified phase index cards. The lattice constant values for each phase and respective fraction can be observed in Table 1, for 2 h and 5 h milling samples. The refinement attained a residual with $CHI^2 = 0.4962$ for 2 h and $CHI^2 = 1.430$ for 5 h, both being acceptable results.

As the milling time increases, so does the FCC phase fraction. Theoretical lattice constant presented in each phase's ICSD card (FCC = 3.588 Å, and BCC = 2.8849 Å) indicate small increases in the lattice in early milling (2 h) and significant change at 5 h. This variation can be attributed to the increase in HEA phase formation, as well as the severe lattice distortion effect, and increased micro strain promoted by MA (Kumar *et al.*, 2022). In Table 2 are presented FWHM values obtained from Lorentzian deconvolution of the diffraction data, crystallite size calculated using Scherrer's formula (Eq. 2), and crystalline fraction was obtained subtracting peak areas from diffraction pattern by peak integration.

Table 1. Lattice constant information, unitary cell volume and phase fractions of MA-HEA as milled.

Sample	Phase and fraction (%)	Lattice constant (Å)	Cell volume (Å^3)
2 h	FCC 65.32	3.5947	46.4502
	BCC 34.68	2.8819	23.9351
5 h	FCC 74.57	3.6434	48.3638
	BCC 25.43	2.9163	24.8025

Table 2. FWHM data from Lorentzian deconvolution and crystallite size calculations from 2 h and 5 h samples.

Sample	Phase	Peak center (2θ °)	FWHM (rad)	Crystallite size (nm)	Crystalline fraction (%)
2 h	FCC	43.43768	0.0193377	8.38	59.2
	BCC	44.40868	0.0123543	12.33	
5 h	FCC	44.31239	0.0156905	11.27	66.4
	BCC	44.58431	0.0137862	12.20	

A crystallite size variation is expected as MA occurs, usually decreasing in size as defects are accumulated and interfacial regions grow in the nanostructure. The 5 h MA-HEA sample shows increased crystallite size for the FCC phase and a slight reduction of the BCC phase. Early milling times provide energy to promote phase formation until the synthetization process ends, reaching phase stabilization. The values observed in the 2 h sample indicate the early synthesis progress is still happening before the severe increase in interfacial component of the nanostructure. This hypothesis can be confirmed by the increase in crystalline fraction at the 5 h mark, but further characterization of longer milling times can conclude this reasoning with higher certainty.

3.2 Laser cladding results

The LC-HEA samples A, B and C where etched using Vilella solution. OM images shown in Figures 4-6 were taken after microhardness indentations and are divided according to each sample: A-(a), B-(b), and C-(c). The first set (Figure 4) shows the general LC-HEA deposition regions, with 50x amplification. The second and third sets, with 400x and 800x amplifications respectively, present general grain morphology, phase development and precipitation microstructures.

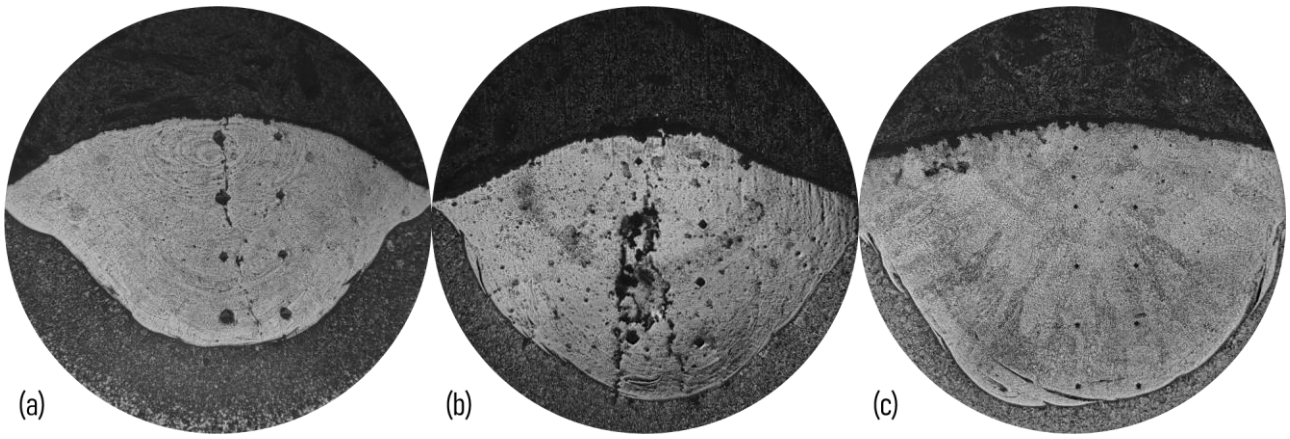

Figure 4. MO with 50x magnification of samples A (a), B (b), and C (c).

At first glance, cracks can be observed in samples A and B, with convection currents visible in A and larger porosity in B. The images were aligned roughly to clarify penetration increase for each power input: 1500 W (a), 2000 W (b), and 2500 W (c).

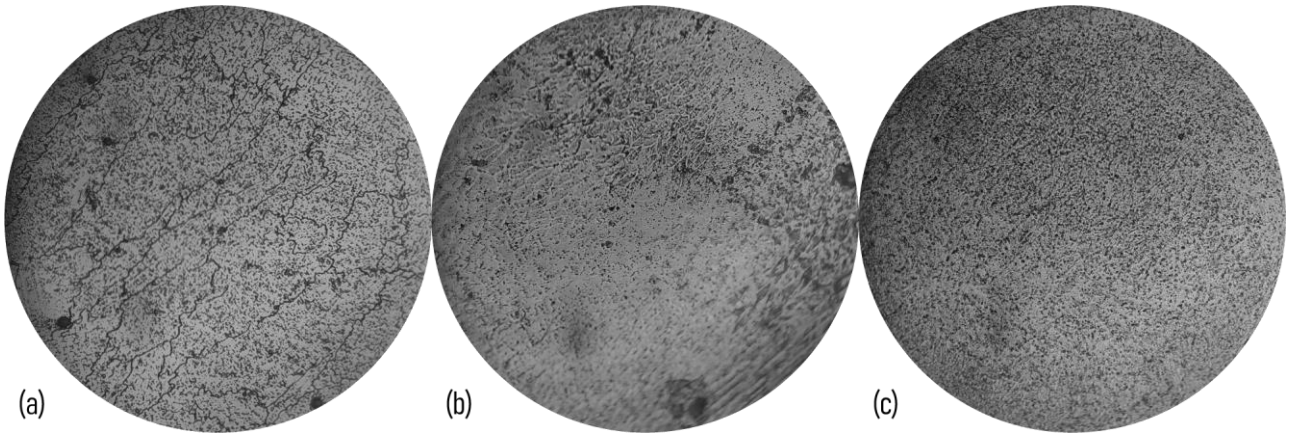

Figure 5. MO with 400x magnification of samples A (a), B (b), and C (c).

As shown in Figure 5, the microstructure becomes finer as the power input increases, with significantly smaller grains. This is counterintuitive considering that with the designated parameters, higher power throughput means higher global temperature, therefore promoting slower cooling and grain growth. In Figure 5 (b), the B sample shows signs of a second phase formation in certain regions, indicating a competition between the two expected phases (BCC and FCC), as grain growth halts when interfaces collide.

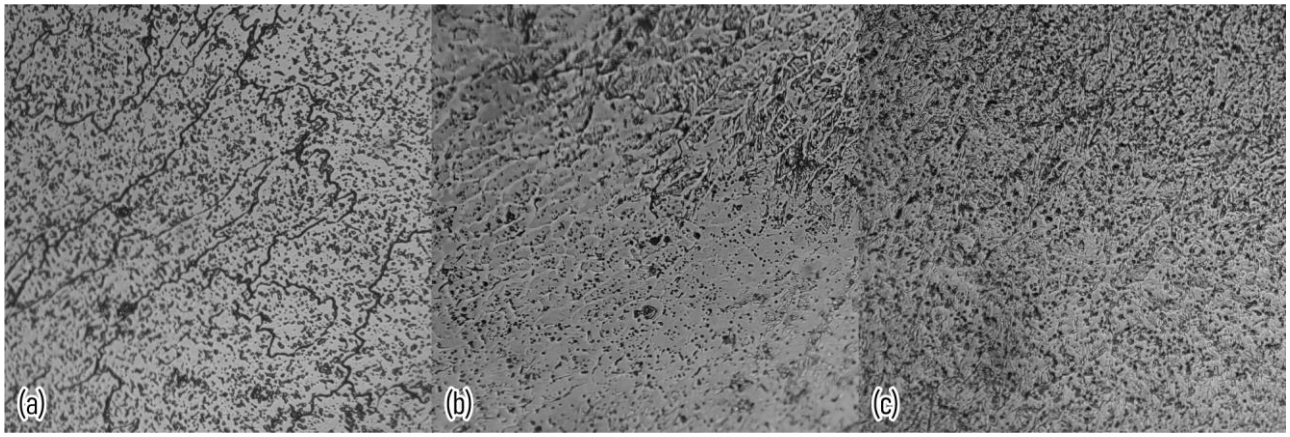

Figure 6. MO with 800x amplification of samples A (a), B (b), and C (c).

With amplification (Figure 6) it's possible to resolve grain boundaries in sample A and identify two distinct phases in B and C samples. Small precipitates can be seen in all samples, but distribution across the structure is more homogenous as power input increases.

Microhardness tests results are provided in Table 3, which also contains a diagram for the tested regions from cross-section samples A, B and C (as previously noted on Figure 1). Two sets of data points were collected linearly, as presented in Table 3, to avoid bias in region selection.

Table 3. Microhardness results for samples A, B, and C of LC-HEA, with positional diagram.

Sample	**A - 1500 W**		**B - 2000 W**		**C - 2500 W**	
Dataset	1 (HV)	2 (HV)	3 (HV)	4 (HV)	5 (HV)	6 (HV)
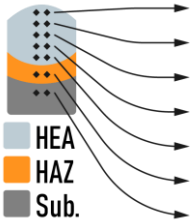	66.6[1]	133,5	177.3	196.0	398.7	382.2
	50.1[1]	132,0	153.7	-[1]	410.0	387.2
	116.9	131,4	149.9	184.8	390.7	371.0
	82.8	85,9	131.8	68.65[1]	376.1	400.3
	-	-	-	-	397.0[2]	396.1[2]
	365.8	264.4	342.7	357.8	244.2	248.1
	200.5	173.2	206.5	186.6	173.3	170.9

[1]Indentation affected by volumetric defects.
[2]Indentations available due to deeper laser penetration.

The microhardness results help understand the mechanical implications of the structures presented (Figures 4-6). Samples A and B have lower hardness when compared to the substrate and HAZ. The values obtained in the MZ have been reported in HEAs with similar compositions (Zhang *et al.*, 2014), and the FCC phase formation can be linked to Cu concentration (Campo *et al*., 2021). Quenching provided by the substrate promotes the stability of FCC phase, greatly increasing ductility, but as the surface and center of the deposition cool at lower rates, the resulting phase equilibrium is changed and, most likely, being responsible for the cracks observed in samples A and B. With increasing BCC phase, sample B becomes sturdier but, with low homogenization, cracks are formed. A better balance is observed in sample C, where BCC+FCC coexistence refines the structure and, with better distribution of precipitation, the overall hardness of C sample reaches an average value of 389.5 HV.

4. CONCLUSIONS

CrMnFeNiCu HEA has been synthesized by MA with 5 h of milling, forming a biphasic structure (BCC+FCC) with higher C_p than the weighted average of the composing elements. The crystallite size changes observed suggest that phase formation is stablished with few milling hours, thus making MA a promising synthesis route for HEA powder feedstock, due to low-cost batch production.

LC-HEA shows two significant distinctions on mechanical properties: with lower energy density a soft monophasic structure was obtained, with hardness under 153.7 HV; whilst higher energy density promoted formation of a fine BCC+FCC structure with homogeneous precipitation and average hardness of 389.5 HV.

The observed defects in the LC-HEA suggest that LC parameters should be revised to obtain a shallower MZ, and further analyses are required to determine phase and precipitation compositions due to dilution effects. Element

mapping by SEM-EDS can provide clear identification of possible regions enriched with Fe from the substrate, and bulk XRD should be executed to identify the precipitation compounds. Lastly, the variation in hardness observed with different energy densities could be applied in contexts requiring mechanical conformation of a ductile structure followed by precipitation hardening promoted by heat treatment, akin to aging in other alloys.

5. ACKNOWLEDGEMENTS

As part of the PPGMAT (Programa de pós-graduação em Ciência e Engenharia de Materiais) we thank CNPq (Conselho Nacional de Desenvolvimento Científico e Tecnológico) and CAPES (Coordenação de Aperfeiçoamento de Pessoal de Nível Superior) for the research financing provided; GESMat (Grupo de Estudo e Síntese de Materiais) colleagues for their cooperation in daily research activities; and UFSC for the laboratory infrastructures available in both Trindade and Blumenau campuses which made this research possible: LMP (Precision Engineering Laboratory), LEM (Mechanical Tests Laboratory), LTE (Thermal Analysis Laboratory), LAMAE (Microscopy and Structural Analysis Laboratory), and LAMAT (Materialography Laboratory).

6. REFERENCES

Arif, Z.U., Khalid, M.Y., Rashid, A.A., Rehman, E. and Atif, M., 2022. Laser deposition of high-entropy alloys: a comprehensive review. *Optics & Laser Technology*, Vol. 145, pp. 107447. DOI: 10.1016/j.optlastec.2021.107447.

ASTM International, 2018. Standard test method for determining specific heat capacity by differential scanning calorimetry. E1269-11. *Annual Book of ASTM Standards*, Vol. 14.01. DOI: 10.1520/E1269-11R18.

ASTM International, 2022. Standard Test method for microindentation hardness of materials. E384-22. *Annual Book of ASTM Standards*, Vol. 3.01. DOI: 10.1520/E0384-22.

Bradley, A.J., Cox, W.F. and Goldschmidt, H.J., 1941. An x-ray study of the Fe-Cu-Ni equilibrium diagram at various temperatures. *Journal of the Institute of Metals*, Vol. 67, pp. 180-201. ICSD #108378.

Campo, K.N., Freitas, C.C., Fonseca, E.B. and Caran, R. 2021. CrCuFeMnNi high-entropy alloys for semisolid processing: The effect of copper on phase formation, melting behavior, and semisolid microstructure. *Materials Characterization*, Vol. 178, pp. 111260. DOI: 10.1016/j.matchar.2021.111260.

Cullity, B.D. and Stock, S.R., 2014. "Elements of X-ray diffraction." Pearson, 3rd ed., 649 p.

Kumar, A., Singh, A. and Suhane, A., 2022. A critical review on mechanically alloyed high entropy alloys: processing challenges and properties. *Materials Research Express*, Vol. 9, pp. 052001. DOI: 10.1088/2053-1591/ac69b3.

Larson, A.C. and Von Dreele, R.B., 2000. General structure analysis system (GSAS). *Los Alamos National Laboratory Report (LAUR)*, pp. 86-748.

Hariharan, K. and Sivaprasad, K., 2022. Sustainable low-cost method for production of high-entropy alloys from alloy scraps. *Journal of Sustainable Metallurgy*, Vol. 8, pp. 625-631. DOI: 10.1007/s40831-022-00523-x.

Murty, B.S., Yeh, J.W., Ranganathan, S. and Bhattacharjee, P.P., 2019. "High-entropy alloys." Elsevier, 2 ed., 363 p.

Ni, H., Zhu, J., Wang, Z., Lv, H., Su, Y. and Zhang, X., 2019. A brief overview on grain growth of bulk electrodeposited nanocrystalline nickel and nickel-iron alloys. *Reviews on Advanced Materials Science*, Vol. 58, pp. 98-106. DOI: 10.1515/rams-2019-0011.

Saud, S.N., Hamzah, E., Abubakar, T. and Farahany, S., 2014. Structure-property relationship of Cu-Al-Ni-Fe shape memory alloys in different quenching media. *Journal of Materials Engineering and Performance*, Vol. 23, pp. 255-261. DOI: 10.1007/s11665-013-0759-9.

Shkodich, N.F., Kovalev, I.D., Kuskov, K.V., Kovalev, D.Y., Vergunova, Y.S., Scheck, Y.B., Vadchenko, S.G., Politano, O., Baras, F., Rogachev, A.S., 2022. Fast mechanical synthesis, structure evolution, and thermal stability of nanostructured CoCrFeNiCu high entropy alloy. *Journal of Alloys and Compounds*, Vol. 893, pp. 161839. DOI: 10.1016/j.jallcom.2021.161839.

Straumanis, M.E. and Weng, C.C., 1956. The absorption and refraction corrections and the lattice constants of chromium. *American Mineralogist*, Vol. 41, pp. 437-448. ICSD #44731.

Zagorac, D., Müller, H., Ruehl, S., Zagorac, J. and Rehme, S. 2019. Recent developments in the Inorganic Crystal Structure Database: theoretical crystal structure data and related features. *Journal of Applied Crystallography*, Vol. 52, pp. 918-925. DOI: 10.1107/S160057671900997X.

Zhang, Y., Zuo, T.T., Tang, Z., Gao, M.C., Dahmen, K.A., Liaw, P.K. and Lu, Z.P., 2014. Microstructures and properties of high-entropy alloys. *Progress in Materials Science*, Vol. 61, pp. 1-93. DOI: 10.1016/j.pmatsci.2013.10.001

7. RESPONSIBILITY NOTICE

The authors are the only responsible for the printed material included in this paper.